Optical Engineering

OpticalEngineering.SPIEDigitalLibrary.org

# Automatic classification of true and false laser-induced damage in large aperture optics

Fupeng Wei
Fengdong Chen
Bingguo Liu
Zhitao Peng
Jun Tang
Qihua Zhu
Dongxia Hu
Yong Xiang
Nan Liu
Zhihong Sun
Guodong Liu

SPIE.

Fupeng Wei, Fengdong Chen, Bingguo Liu, Zhitao Peng, Jun Tang, Qihua Zhu, Dongxia Hu, Yong Xiang, Nan Liu, Zhihong Sun, Guodong Liu, "Automatic classification of true and false laser-induced damage in large aperture optics," *Opt. Eng.* **57**(5), 053112 (2018), doi: 10.1117/1.OE.57.5.053112.

# Automatic classification of true and false laser-induced damage in large aperture optics

**Fupeng Wei,[a,b,†] Fengdong Chen,[a,*,†] Bingguo Liu,[a] Zhitao Peng,[b] Jun Tang,[b] Qihua Zhu,[b] Dongxia Hu,[b] Yong Xiang,[b] Nan Liu,[b] Zhihong Sun,[b] and Guodong Liu[a,*,†]**
[a]Harbin Institute of Technology, School of Electrical Engineering and Automation, Nangang District, Harbin, China
[b]China Academy of Engineering Physics, Research Center of Laser Fusion, Youxian District, Mianyang, China

**Abstract.** An automatic classification method based on machine learning is proposed to distinguish between true and false laser-induced damage in large aperture optics. First, far-field light intensity distributions are calculated via numerical calculations based on both the finite-difference time-domain and the Fourier optical angle spectrum theory for Maxwell's equations. The feature vectors are presented to describe the possible damage sites, which include true and false damage sites. Finally, a kernel-based extreme learning machine is used for automatic recognition of the true sites and false sites. The method studied in this paper achieves good recognition of false damage, which includes a variety of types, especially attachment-type false damage, which has rarely been studied before.  [DOI: 10.1117/1.OE.57.5.053112]

Keywords: laser-induced damage; finite-difference time-domain; feature vector; kernel-based extreme learning machine.

Paper 171762 received Nov. 4, 2017; accepted for publication Apr. 26, 2018; published online May 24, 2018.

## 1 Introduction

A final optics assembly (FOA) is located at the output end of an inertial confinement fusion (ICF) experimental device. There are 48 FOAs in the Shenguang-III (SG-III) laser facility, each containing nine large aperture optics, the aperture size of which is 430 mm × 430 mm. Laser-induced damage is easily generated under 351-nm high-power laser irradiation.[1–3] When the number of damaged sites increases to a certain magnitude, these sites modulate the high-power UV lasers in ICF experiments, thereby significantly affecting the beam quality.[4–7] The best way to rapidly and efficiently detect and track the damage on an FOA surface is to design an online imaging system for observing tiny defects in the center of the target chamber. From the literature published in recent years, there are mainly two research teams in the field of damage online detection in ICF experiments for large aperture optics: the Lawrence Livermore National Laboratory (LLNL) and the China Academy of Engineering Physics (CAEP). Each team has developed its own experimental version of the final optics damage inspection (FODI) system, namely, the NIF FODI developed for the United States National Ignition Facility (NIF) by LLNL scientists[8,9] and the SG-III FODI we developed for the SG-III laser facility at the CAEP.[10] In general, FODI is an online imaging system based on machine vision for rapidly observing laser-induced damage. With edge illumination technology in the dark field, FODI captures images of the damage on an FOA surface and obtains the damage information by image processing. LLNL scientists have conducted much meaningful research in this field. Kegelmeyer et al.[11] used the local area signal-to-noise ratio (LASNR) algorithm to process FODI images to obtain all possible damage sites; these sites are also called candidate sites or LASNR markers. The FOA damage condition can be roughly obtained using these LASNR markers. However, due to the presence of stray light, a significant amount of noise is present in FODI images in addition to true damage, as shown in Fig. 1(b), which is referred to as false damage.[6,12,13] These candidate sites can generally be divided into these categories: damage site, hardware reflection (HR), damaged CCD pixels (DC), reflection of a damage site (RD), and attachments (Att).[14] Damage sites are also called true damage sites or true sites, and the others are called false damage sites or false sites. How to accurately remove all kinds of false damage while retaining the true damage is a hot and challenging topic in the present research. Abdulla et al. conducted machine learning of an ensemble of decision trees to identify HR-type false sites from LASNR markers with very high accuracy (99.8%, 10-fold crossvalidation). After the removal of HR-type sites, the remaining false sites (Abdulla et al.[15] referred to them as being of the unknown type, here abbreviated as UN-type) and true sites were mixed together. DC-type false sites are caused by radiation or thermal noise generated by long-term operation in a vacuum environment and generally appear as randomly distributed isolated pixels with high gray values. These DC can be easily identified via machine learning or other pattern recognition methods. To save time for later machine learning classifications, we have identified these pixels in the data-preprocessing step and removed them from the FODI image. RD-type false sites are also easy to identify and will be discussed in Sec. 2.1. Att-type false sites are more similar to true sites than any other types of false site when observed by the naked eye. The traditional machine learning methods often struggle to identify them, and almost no related studies exist in the field of damage

*Address all correspondence to: Fengdong Chen, E-mail: chenfd@hit.edu.cn; Guodong Liu, E-mail: lgd@hit.edu.cn

†Authors contributed equally to this work.

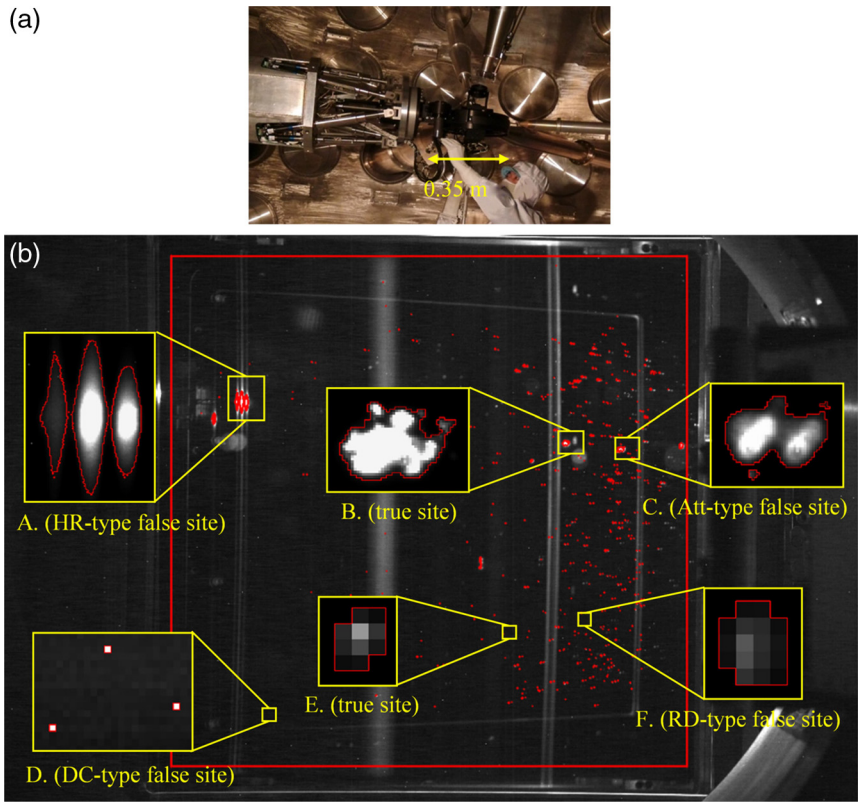


**Fig. 1** The SG-III FODI system, with the LASNR of each false and true damage sites indicated in the FODI online image. (a) SG-III FODI system, which we developed for the SG-III laser facility at the CAEP; it is also the experimental device used in our paper. (b) True and false damage sites in an SG-III FODI online image.

online inspection. To solve this problem, we establish our FODI detection system in the SG-III laser facility and present a new solution for the classification of true and false sites. Limited by the size of the workspace, the SG-III FODI system is smaller than the NIF FODI system, as shown in Fig. 1(a); its size is 0.35 m. The SG-III FODI system obtains online images in a vacuum target chamber, in which the distance between the FOA and FODI camera usually ranges from 3.7 to 5.1 m. This system can detect damage larger than 100 $\mu$m with a sizing accuracy of at most $\pm 15\%$ and damage ranging from 50 to 100 $\mu$m with a sizing accuracy of at most $\pm 30\%$. For convenience of description, FODI is herein used to refer to SG-III FODI unless specified as NIF FODI.

The goal is to combine all false sites together as one type, identifying and removing all of them simultaneously rather than identifying only one false site type or leaving other false site types to be mistaken for true sites. The categories, causes, and solutions of the candidate sites are summarized in Table 1. To propose a new solution, we analyze the optical principles of the generation of false damage and true damage and the differences in the optical features of their images generated by a CCD. The simulation and experiment reveal that the light leakage caused by edge illumination forms stray light, which is an important factor of the appearing of HR-type, RD-type, and Att-type false sites in FODI images. As shown in Fig. 1(b), the illuminated border on the adjacent optics, the unmarked white strip, and the large bright spot are all false sites. In this work, the greatest challenge is to identify Att-type false sites. To effectively distinguish them, this paper analyzes their scattering and imaging features. Since a scratch is a lengthened pit, we need to analyze only the luminous characteristics of a pit. The true damage sites are shown in Fig. 1(b), e.g., sites B and E. Finally, we use machine learning to perform high-accuracy classification experiments on false and true damage.

**Table 1** The types, causes, and solutions of candidate sites.

| | Type | Cause | Solution |
|---|---|---|---|
| True | Pit | High-power laser irradiation | Feature vector and K-ELM |
| False | HR | FOA inner metal wall or adjacent optics illuminated by stray light | |
| | RD | Defects on adjacent optics illuminated by stray light | |
| | Att | Attachments illuminated by stray light | |
| | DC | Radiation or thermal noise generated during long-term operation in a vacuum environment | Preprocessing |

## 2 Analysis of True and False Damage Characteristics

### 2.1 *Reason for the Occurrence of False Damage*

An FODI system uses edge illumination as an imaging technology.[8,16,17] As shown in Fig. 2, all optics have two microlaser diodes (MLDs) fixed in a metal frame as the illumination light source. Two cases are shown in Figs. 2(a) and 2(b), in which the MLD illumination light wavelength is 808 nm, the divergence angle is 70 deg, and the degree of light polarization is 0.9. In the case of a fused silica material vacuum separator, the size is 430 mm × 430 mm × 10 mm. For a nondamaging optic, the light emitted from the MLD is irradiated onto its surface, and the total internal reflection (TIR) propagates through the optic. When light is transmitted to the other border of the optic, the TIR condition is disrupted, and light scatters to the outside.[18] This is the main cause of stray light. Using the Monte Carlo ray-tracing method in the TracePro simulation software (Lambda Research Corporation, Littleton, Massachusetts), the optical energy radiating outward (front, back, left, right, up, and down) from the optics can be calculated. As shown in Figs. 2(c) and 2(d), monitors of the front, back, left, right, up, and down radiation are set outside the optics. We can calculate the optical power incident on each monitor. For convenience, Figs. 2(c) and 2(d) show 2.5% of the total simulated light.

When the single MLD light power is 1.579 W, the power $P_i$ injected into the optic is $2 \times 1.579$ W. The data corresponding to the incident light power on each position monitor ($P_{left}$, $P_{right}$, $P_{front}$, $P_{back}$, $P_{up}$, and $P_{down}$), the total power radiated outward [$P_o$, as shown in Eq. (1)], and the fraction of leakage power ($P_o/P_i$) are shown in Table 2.

$$P_o = P_{left} + P_{right} + P_{front} + P_{back} + P_{up} + P_{down}. \quad (1)$$

The data presented in Table 2 show that the power of leaked light accounts for nearly 1/4 of the luminous power of the two MLDs. This leaked light interferes with FODI imaging. In the FOA presented in Fig. 3, two damage sites are shown: pit types A and B on optic1 and optic2. In addition, a fused silica particle of Att-type C is shown in optic2. The FODI system uses time-division-multiplexing-independent edge illumination technology; thus, if the inspected optic is optic2, only the MLDs on the optic2 edge illumination light source are turned on, whereas the MLDs on the others optics are turned off. Stray light leaked from optic2 will be reflected onto the final inner metal wall or adjacent optics3; A and C may also be illuminated by this stray light. Although A represents true damage on optic1, it is false damage for optic2 in the FODI image. For this false damage, which Spaeth et al.[14] called the reflection of a damage site (RD-type false site), we can adjust the FODI camera lens so that its imaging is blurry and easy to distinguish using a machine learning classifier. For the case of C, if the contact area between C and the optic surface is small and no extraneous stray light exists, C will not appear in the FODI image. When extraneous stray light irradiates C, an Att-type false site will appear in the FODI image of optic2.

### 2.2 *Far-Field Light Intensity Features of True and Att-Type False Damage*

For optic2, our experimental results indicate that the pit depth $h$ is approximately one-fifth the lateral diameter $d$. Assuming that the damage section of the pit is a smooth arc or a burr arc, fused silica debris attachments are divided

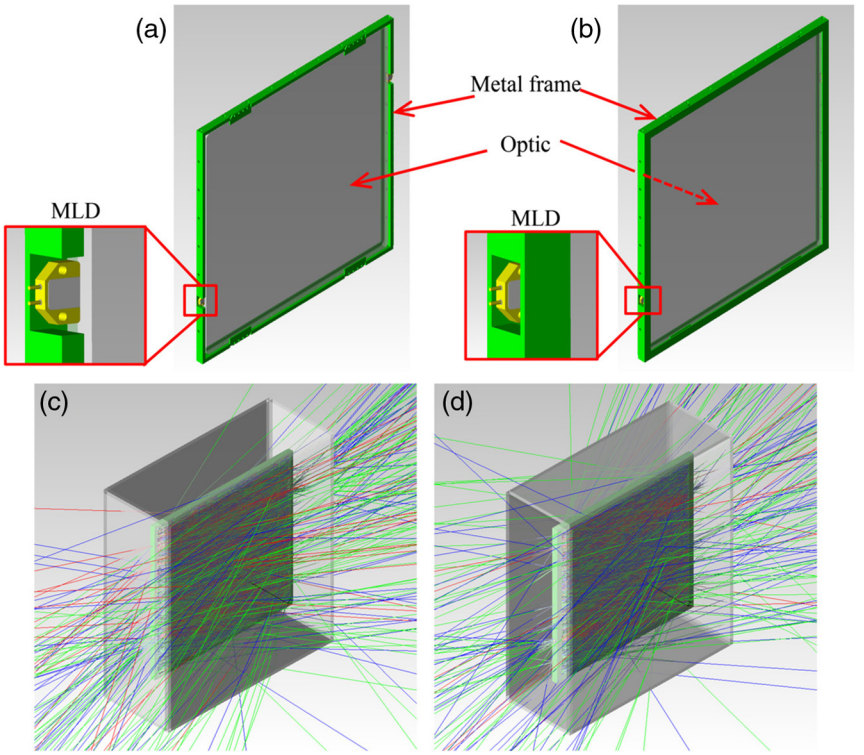


**Fig. 2** Two illumination modes showing light leakage. (a) Illumination mode 1. (b) Illumination mode 2. (c) Light leakage of mode 1. (d) Light leakage of mode 2.

**Table 2** Light power in all directions measured by the monitors ($W$).

| Monitor | $P_i$ | $P_{left}$ | $P_{right}$ | $P_{front}$ | $P_{back}$ | $P_{up}$ | $P_{down}$ | $P_o$ | $P_o/P_i$ |
|---|---|---|---|---|---|---|---|---|---|
| Mode 1 | 3.16 | 0.16 | 0.19 | 0.42 | 0 | 0.03 | 0.02 | 0.82 | 25.94% |
| Mode 2 | 3.16 | 0.15 | 0.19 | 0.19 | 0.17 | 0.02 | 0.02 | 0.75 | 23.70% |

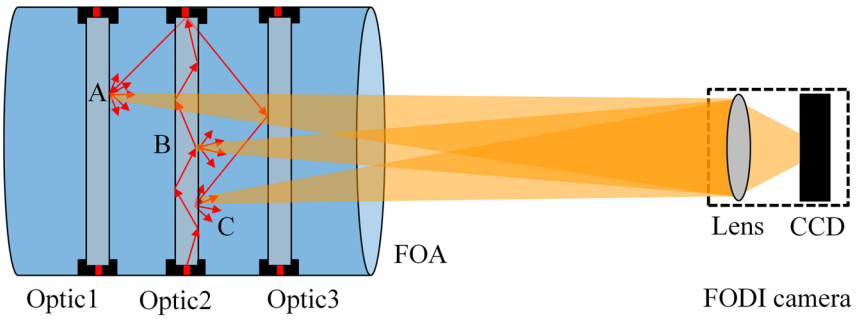


**Fig. 3** True damage and false damage (RD-type and Att-type) generated in FODI image.

into two types: the $Att_1$-type, which is symmetrical with respect to the pit, and the $Att_2$-type with an elliptical section. The two-dimensional (2-D) physical topography and the sizes of pit, $Att_1$ and $Att_2$ are shown in Fig. 4. If the amplitude of the internal reflection lighting S is set to 1.0, the incidence angle range is 0 deg to 23.24 deg; if the amplitude of the stray light N is 0.5, then the incidence angle range is 0 deg to 38.36 deg (the incidence angle ranges of S and N can be calculated using TracePro). The illuminations of pit, $Att_1$, and $Att_2$ are divided into the cases shown in Fig. 4. 2-D simulation analyses of the intensity distributions of pit, $Att_1$, and $Att_2$ at the position of the imaging lens and the CCD surface are numerically calculated by the finite-difference time-domain (FDTD) method and Fourier optic angle spectrum theory (AST).[19,20]

The far-field intensity distributions at the FODI camera lens of pit, $Att_1$, and $Att_2$ are simulated using the FDTD method in different illumination modes. The light intensity distributions at the CCD surface are calculated using the Fourier optic AST.[20–22] The intensity distribution curves for the smooth-shaped pit, $Att_1$, and $Att_2$ are shown in Fig. 5. The light intensity distribution curves for the burr-shaped pit, $Att_1$, and $Att_2$ are shown in Fig. 6.

Suppose that the maximum light intensity value of the CCD in Figs. 5(b), 5(d), 6(b), and 6(d) is $v_{max}$, $v_1 = 0.1v_{max}$, and $v_2 = 0.9v_{max}$, $L$ is the total interval length along the $x$-axis, $L_1$ is the interval length of the light intensity value greater than $v_1$, and $L_2$ is the interval length of the light intensity value greater than $v_2$. We refer to the light intensity illuminated only with S as the signal light intensity and the light intensity illuminated with S and N as the mixed light intensity. An examination of Figs. 5(b), 5(d), 6(b), and 6(d) shows that the light intensity distributions of the pit and attachments differ, especially at the CCD surface, and that this difference can be represented by a series of features defined as follows: (1) effective light interval ratio $[z^{(1)}]$,

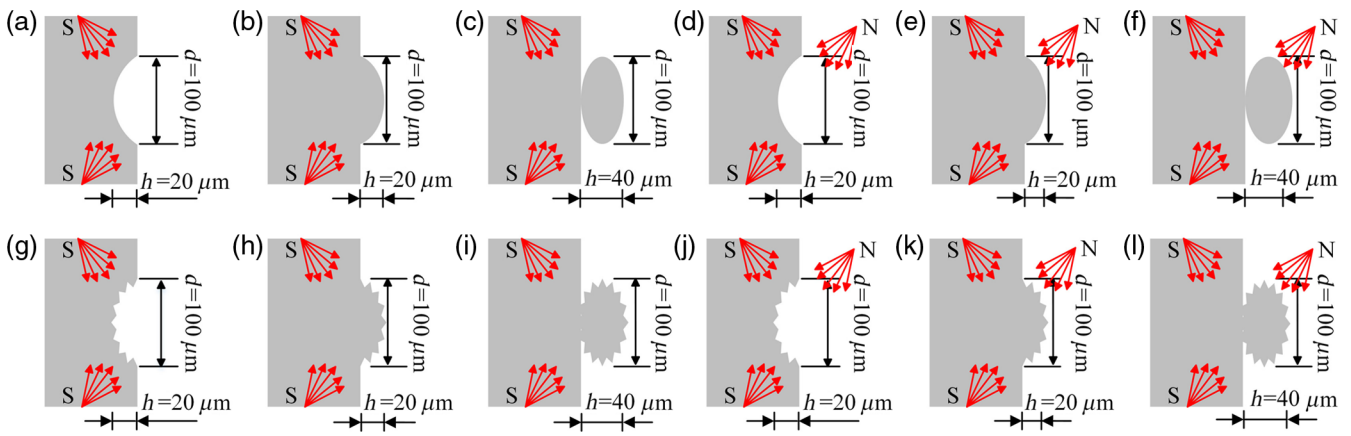


**Fig. 4** 2-D topography and illumination conditions for pit, $Att_1$, and $Att_2$. (a) Smooth arc pit (S). (b) Smooth arc $Att_1$ (S). (c) Smooth ellipse $Att_2$ (S). (d) Smooth arc pit (S + N). (e) Smooth arc $Att_1$ (S + N). (f) Smooth ellipse $Att_2$ (S + N). (g) Burr arc Pit (S). (h) Burr arc $Att_1$ (S). (i) Burr ellipse $Att_2$ (S). (j) Burr arc Pit (S + N). (k) Burr arc $Att_1$ (S + N). (l) Burr ellipse $Att_2$ (S + N).

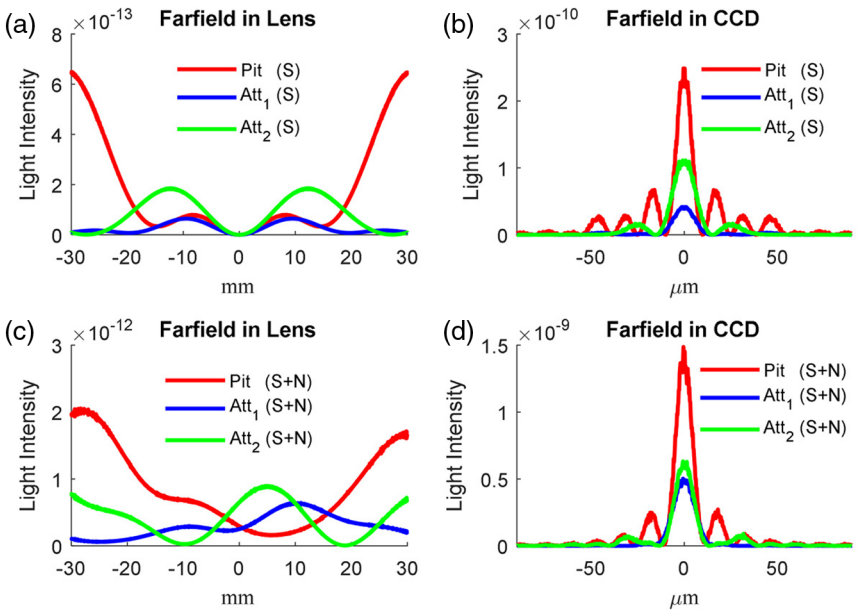


**Fig. 5** Light intensity distribution curves for the smooth-shaped pit, $Att_1$, and $Att_2$. (a) Illumination with S. (b) Illumination with S. (c) Illumination with S and N. (d) Illumination with S and N.

which is $L_1/L$; (2) sum of the signal light intensities $[z^{(2)}]$; (3) sum of the noise light intensities $[z^{(3)}]$; (4) average value of the signal light intensity $[z^{(4)}]$; (5) variance of the signal light intensity $[z^{(5)}]$; (6) average value of the noise light intensity $[z^{(6)}]$; (7) maximum value of the signal light intensity $[z^{(7)}]$; (8) maximum value of the noise light intensity $[z^{(8)}]$; (9) sum of the LASNR values $[z^{(9)}]$; (10) signal-to-noise light energy ratio $[z^{(10)}]$; (11) saturated light interval ratio $[z^{(11)}]$, which is $L_2/L$; and (12) saturated light energy ratio $[z^{(12)}]$. These 12 features $[z^{(1)}, \ldots, z^{(12)}]$ illustrate the difference between Att-type false damage and true damage from the perspective of simulation. Hence, these 12 features in the simulation provide the theoretical basis for extracting features from FODI images. For example, for the burr-shaped pit and attachments, if we combine Figs. 6(b) and 6(d), we can obtain the new figure shown in Fig. 7.

Figure 7 shows that due to the presence of stray light N, the mixed light intensity is higher than the corresponding signal light intensity. The noise light intensity can be obtained by subtracting the signal light intensity from the mixed light intensity. We suppose that a baseline exists in Fig. 7 and that the curve above the baseline can cause the CCD pixels to produce photoelectric induction. In the

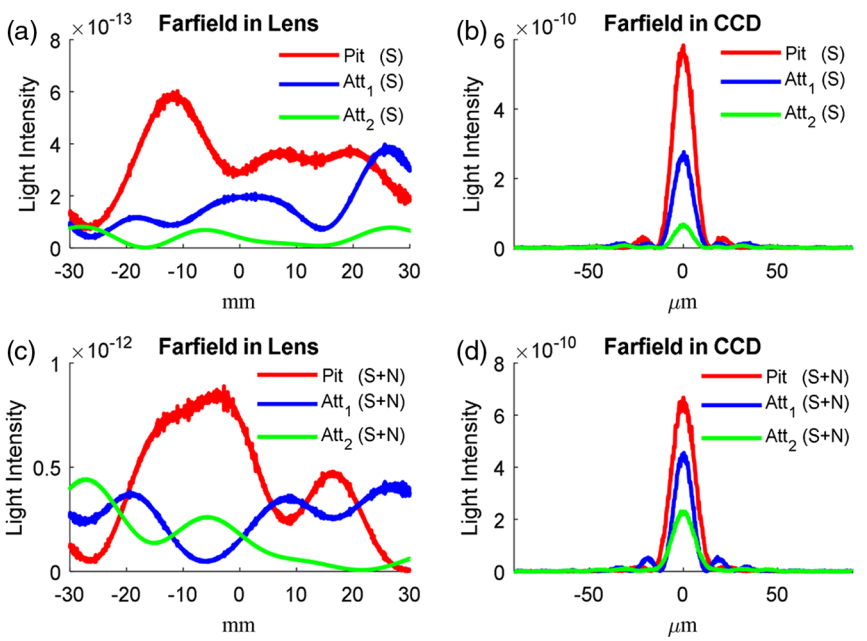


**Fig. 6** Light intensity distribution curves for the burr-shaped pit, $Att_1$, and $Att_2$. (a) Illumination with S. (b) Illumination with S. (c) Illumination with S and N. (d) Illumination with S and N.

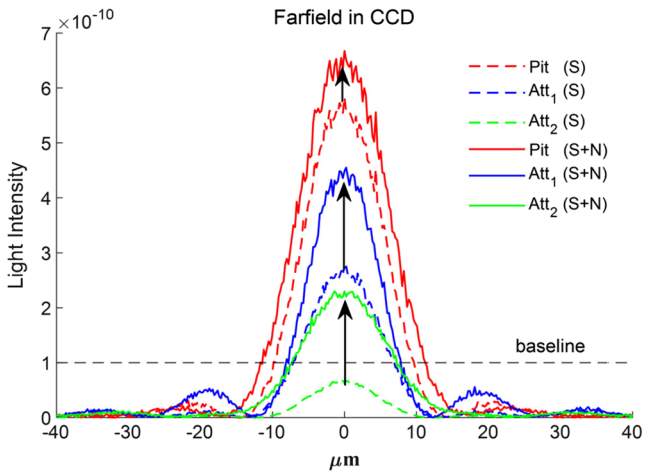


**Fig. 7** Light intensity distribution curves for the burr-shaped pit, $Att_1$, and $Att_2$.

case of illumination with S or S + N, the interval of pit above the baseline is always longer than that of $Att_1$ and $Att_2$. This means that a pit can form a larger spot on a CCD than attachments when they have the same size. For the curves above the baseline, the curve of pit is higher than that of $Att_1$ and $Att_2$. This means that a pit can form a brighter spot on a CCD than attachments when they have the same size. In other words, the difference in $z^{(1)}$ between the pit and attachments will result in different bright spot sizes on the CCD, the difference in $z^{(2)}$ between the pit and attachments will result in different sums of the pixel gray values of the spot signal on the CCD, and so on. A comparison of these features $[z^{(1)}, \ldots, z^{(12)}]$ for the burr-shaped pit, $Att_1$, and $Att_2$ in the optical simulation is shown in Table 3.

**Table 3** Pit and attachment features of light intensity simulation and FODI images.

| FDTD + AST simulation | | | | FODI experiment | | |
|---|---|---|---|---|---|---|
| No. | Pit | $Att_1$ | $Att_2$ | No. | Pit | Att |
| $z^{(1)}$ | 0.35 | 0.24 | 0.20 | $x^{(1)}$ | 5 | 4 |
| $z^{(2)}$ | $8.6\times10^{-8}$ | $4.1\times10^{-8}$ | $1.1\times10^{-8}$ | $x^{(2)}$ | 148,225 | 33,811 |
| $z^{(3)}$ | $1.1\times10^{-8}$ | $1.6\times10^{-8}$ | $3.1\times10^{-8}$ | $x^{(3)}$ | 19,605 | 9535 |
| $z^{(4)}$ | $3.3\times10^{-13}$ | $1.6\times10^{-13}$ | $4.1\times10^{-14}$ | $x^{(4)}$ | 29,645 | 8453 |
| $z^{(5)}$ | $5.2\times10^{-23}$ | $1.1\times10^{-23}$ | $5.9\times10^{-25}$ | $x^{(5)}$ | 8497 | 5189 |
| $z^{(6)}$ | $4.3\times10^{-14}$ | $6.1\times10^{-14}$ | $1.2\times10^{-13}$ | $x^{(6)}$ | 3921 | 2384 |
| $z^{(7)}$ | $5.8\times10^{-10}$ | $2.8\times10^{-10}$ | $6.8\times10^{-11}$ | $x^{(7)}$ | 37,721 | 17,277 |
| $z^{(8)}$ | $6.2\times10^{-11}$ | $9.7\times10^{-11}$ | $2.1\times10^{-10}$ | $x^{(8)}$ | 3924 | 2388 |
| $z^{(9)}$ | 9354 | 2953 | 377 | $x^{(9)}$ | 309 | 69 |
| $z^{(10)}$ | 7.7 | 2.58 | 0.35 | $x^{(10)}$ | 61 | 17 |
| $z^{(11)}$ | 0.17 | 0 | 0 | $x^{(11)}$ | 0 | 0 |
| $z^{(12)}$ | 0.24 | 0 | 0 | $x^{(12)}$ | 0 | 0 |
| — | — | — | — | $x^{(13)}$ | 2.83 | 2.31 |
| — | — | — | — | $x^{(14)}$ | 1.73 | 1.33 |

### 2.3 *True and Att-Type False Damage in an FODI Image*

In the SG-III laser facility damage inspection experiment, $Att_1$ and $Att_2$ are attributed to Att-type false damage; they are also UN-type false sites, as mentioned in the introduction. An FODI system is used to collect the images under the same illumination conditions and with a pit and an attachment located on the same optic surface. The pit and attachment are ∼100 $\mu$m in size, and their images are shown in Fig. 8.

An FODI image is usually considered to be the superposition of a signal image and a noise image. The signal image can be obtained by processing an FODI image using a Gaussian high-pass filter, whereas the noise image can be obtained by processing FODI images using a Gaussian low-pass filter.[10,11] According to the 12 feature parameters of the light intensity distribution on the CCD surface in the simulation formed by pit, $Att_1$, and $Att_2$, we present the 12 parameters that correspond to the former parameters for describing true and false damage in the experimental FODI images: (1) area (in pixels) in the FODI image, which corresponds to the effective light interval ratio in the simulation $[x^{(1)} \sim z^{(1)}]$; (2) sum of the intensities in the signal image, which corresponds to the sum of the signal light intensities $[x^{(2)} \sim z^{(2)}]$; (3) sum of the intensities in the noise image, which corresponds to the sum of the noise light intensities $[x^{(3)} \sim z^{(3)}]$; (4) signal mean, which corresponds to the average value of the signal light intensity $[x^{(4)} \sim z^{(4)}]$; (5) standard deviation of the pixel values in the signal image, which corresponds to the variance of the signal light intensity $[x^{(5)} \sim z^{(5)}]$; (6) noise mean, which corresponds to the average value of the noise light intensity $[x^{(6)} \sim z^{(6)}]$; (7) maximum pixel intensity value in the signal image, which corresponds to the maximum value of the signal light intensity $[x^{(7)} \sim z^{(7)}]$; (8) maximum pixel intensity value in the noise image, which corresponds to the maximum value of the noise light intensity $[x^{(8)} \sim z^{(8)}]$; (9) sum of the LASNR values, which corresponds to the sum of the LASNR values $[x^{(9)} \sim z^{(9)}]$; (10) ratio of signal energy-to-noise energy, which corresponds to the signal-to-noise light energy ratio $[x^{(10)} \sim z^{(10)}]$; (11) saturation area ratio, which corresponds to the saturated light interval ratio $[x^{(11)} \sim z^{(11)}]$; and (12) saturation intensity ratio, which corresponds to the saturated light energy ratio $[x^{(12)} \sim z^{(12)}]$. To describe the morphological differences between the pit and attachment in the FODI image, we add two more features: long axis of best fit ellipse $[x^{(13)}]$ and short axis of best fit ellipse $[x^{(14)}]$. For example, a comparison of these features $[x^{(1)}, \ldots, x^{(14)}]$ for the burr-shaped pit and attachment in the FODI images shown in Figs. 8(c) and 8(d) is shown in Table 3.

Under constant illumination conditions, the differences in the pit and attachment in an FODI image can be characterized by $[x^{(1)}, \ldots, x^{(14)}]$, that is, we can use 14 features to distinguish between false sites and true sites with an appropriate mathematical model. Because the SG-III FODI system uses

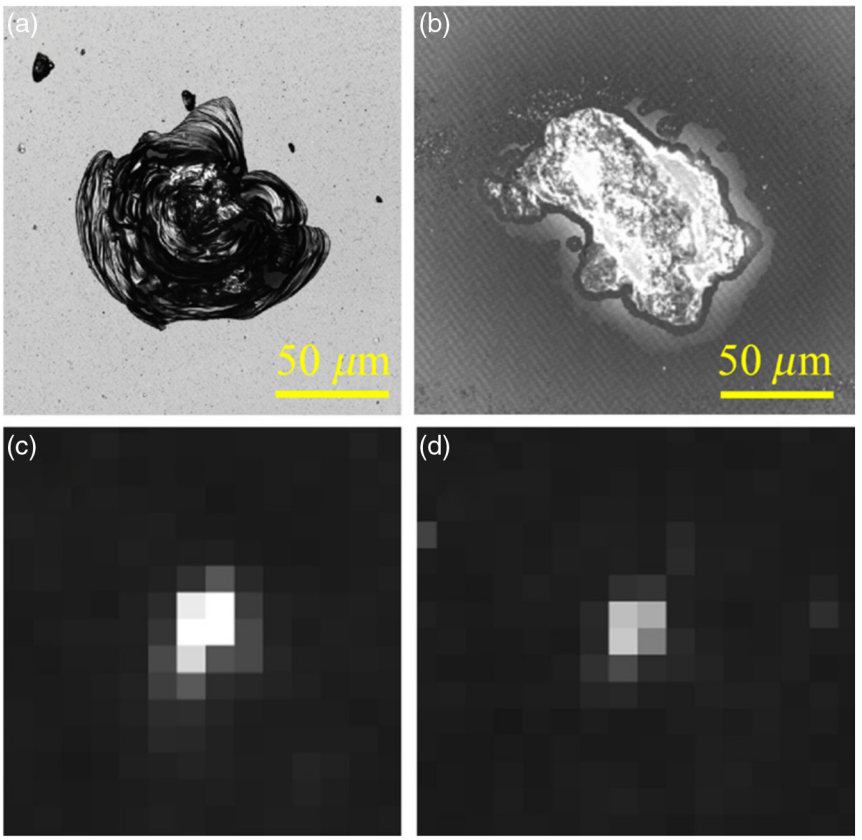


**Fig. 8** True and false damage formed by the pit and attachment. (a) The pit observed under a microscope. (b) The attachment observed under a microscope. (c) The pit observed in an FODI image. (d) The attachment observed in an FODI image.

edge illumination technology, it is affected by the inhomogeneity of the light field distribution within the optics. Using TracePro simulations, we can obtain the internal light intensity distribution, as shown in Fig. 9. When the same shape flaw is located at different locations on the optic surface, the scattered light energy generally appears to be different, which causes variations in the light energy scattered to the CCD; therefore, images with different brightness values are generated. To express differences in the imaging caused by this uneven illumination, image coordinates $(X, Y)$ should be added, with $x^{(15)} = X$ and $x^{(16)} = Y$, and a total of 16 features constitute the feature vector $\mathbf{x}_i = [x_i^{(1)}, \ldots, x_i^{(16)}]^{\mathrm{T}}$ for describing the $i$'th LASNR marker in the FODI image.

## 3 Automatic Classification Method and Experimental Results

Machine learning is an effective method for managing complex classification problems. In this paper, we use the kernel-based extreme learning machine (K-ELM) to solve the automatic classification problem for true and false damage.[23–25] The K-ELM is a fast learning algorithm for single-hidden-layer neural networks, and compared with traditional machine learning methods, such as the error backpropagation neural network (BPNN) and support vector machine (SVM), it has the advantage of being able to perform rapid learning and to obtain highly accurate results.[26,27]

The K-ELM classification model we used in this paper is as follows:

$$f(\mathbf{x}) = \begin{bmatrix} K(\mathbf{x}, \mathbf{x}_1) \\ \vdots \\ K(\mathbf{x}, \mathbf{x}_M) \end{bmatrix}^{\mathrm{T}} \left( \frac{\mathbf{I}}{C} + \mathbf{\Omega}_{\mathrm{train}} \right)^{-1} \mathbf{T}. \tag{2}$$

Here, $K(\mathbf{x}, \mathbf{x}_i)$ is the kernel function, $\mathbf{x} = [x^{(1)}, \ldots, x^{(16)}]$ is the input sample site to be classified, $\mathbf{x}_i = [x_i^{(1)}, \ldots, x_i^{(16)}]$ $(i = 1, \ldots, M)$ is the training sample site, $M$ is the number of all training samples, $\mathbf{I}$ is the unit matrix, $C$ is a constant, $\mathbf{\Omega}_{\mathrm{train}}$ is a kernel matrix composed of training samples, $(\mathbf{\Omega}_{\mathrm{train}})_{i,j} = K(\mathbf{x}_i, \mathbf{x}_j)$, $(i, j = 1, \ldots, M)$, and $\mathbf{T} = [y_1, \ldots, y_M]^{\mathrm{T}}$ is a column vector composed of the class labels of the training samples. In our experiment, $K(\mathbf{x}, \mathbf{x}_i) = \exp(-\gamma \|\mathbf{x} - \mathbf{x}_i\|^2)$, with $\gamma$ being a constant. The machine learning classification process for the identification of true or false damage is shown in Fig. 10.

The K-ELM is a supervised learning method. The training data consist of a set of samples, with each sample being a pair consisting of a feature vector $\mathbf{x}_i$ and a class label $y_i$ (also called the type of site). We match the FODI offline image to the FODI online image to complete the collection of samples. Detailed steps, as well as an example of our experiment, are as follows:

Step 1: Collect the FODI online image of an inspected optic vacuum isolator, mark all possible damage sites using the LASNR algorithm, as shown in Fig. 11(a), and characterize these markers with a feature vector $\mathbf{x}_i$. We refer to these sites as online sites.

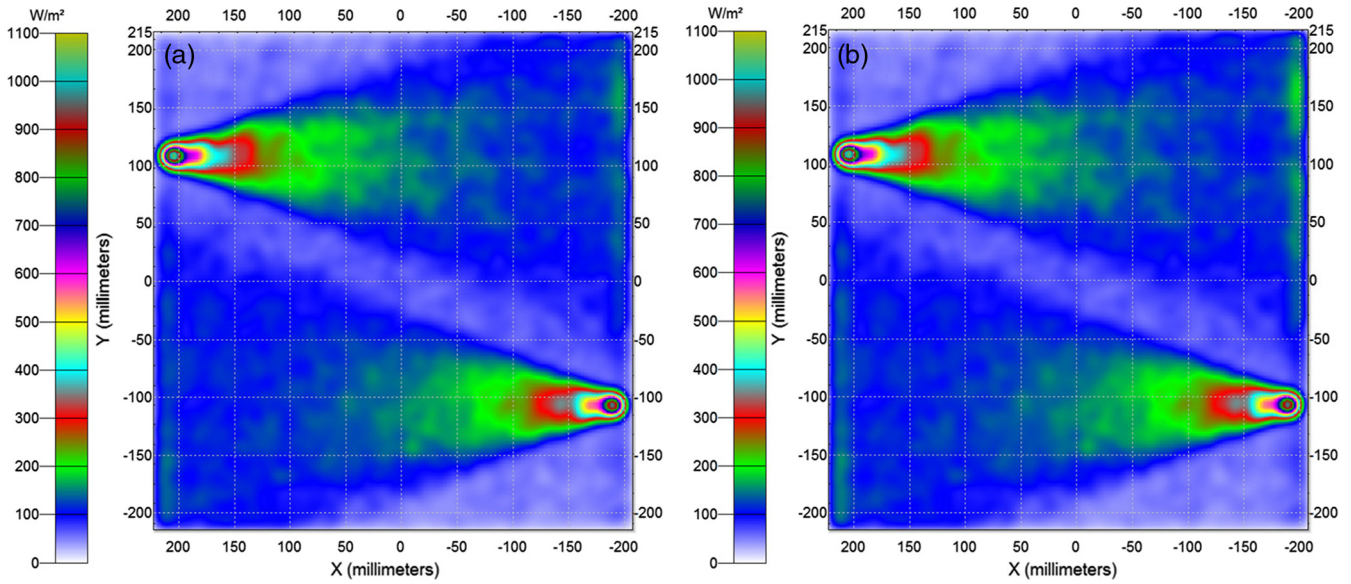


**Fig. 9** Light intensity distribution at the inner optic surface. (a) Light intensity distribution at the inner optic surface under illumination mode 1. (b) Light intensity distribution at the inner optic surface under illumination mode 2.

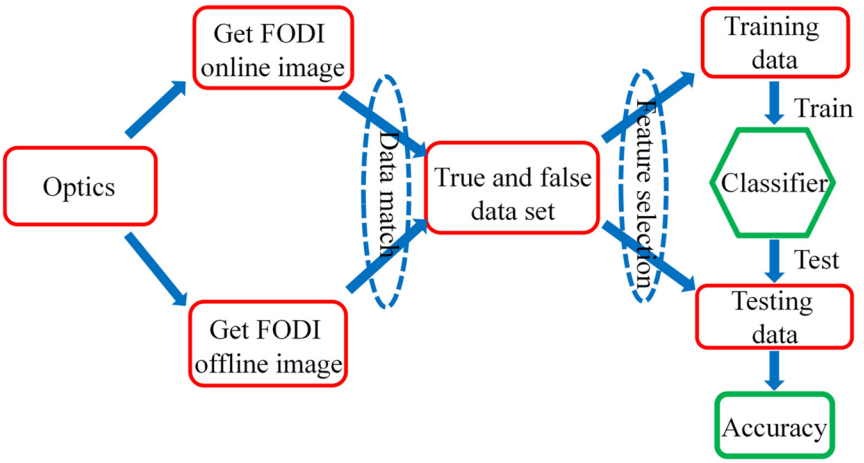


**Fig. 10** True or false damage classification process using a machine learning classifier.

Step 2: Remove the inspected optic vacuum isolator from the SG-III laser facility and place it in a nondisturbing light environment after cleaning the attachments on its surface. Use the FODI offline system to collect an offline image, and mark all sites (referred to as offline sites) using the LASNR algorithm, as shown in Fig. 11(b). Since the attachments have been cleaned away, Att-type false sites do not appear in Fig. 11(b). HR-type false sites are also not generated in the offline image in the nondisturbing light environment; hence, all the offline sites can be considered to be true damage sites.

Step 3: Perform a geometric transformation to match the offline sites to the online sites. The sites in the FODI online image that can be matched with offline sites represent true damage sites; the other sites in the FODI online image that cannot be matched with offline sites represent false damage sites. As shown in Fig. 12, after matching, we obtain false sample sites and true sample sites. Moreover, let $y_i = 1$ for the $i$'th true online site and $y_i = -1$ for the $i$'th false online sites; thus, all online sites can be recorded as $T = \{(\mathbf{x}_i, y_i) | \mathbf{x}_i \in \mathbf{R}^{16}, y_i = \pm 1, i = 1, \ldots, P\}$. We randomly divide the sample $T$ into two parts: $T_{\text{train}}$ and $T_{\text{test}}$. The training data set is $T_{\text{train}} = \{(\mathbf{x}_i, y_i) | \mathbf{x}_i \in \mathbf{R}^{16}, y_i = \pm 1, i = 1, \ldots, M\}$, and the testing data set is $T_{\text{test}} = \{(\mathbf{x}_i, y_i) | \mathbf{x}_i \in \mathbf{R}^{16}, y_i = \pm 1, i = 1, \ldots, N\}$; here, $M = N = P/2$.

Step 4: Use the K-ELM to conduct learning on the training data set $T_{\text{train}}$. Then, optimize the parameters $(C, \gamma)$, as shown in Fig. 13.

Step 5: Use the K-ELM classifier with the optimized parameters $(C^*, \gamma^*)$ after training to verify the classification accuracy rate on the testing data set $T_{\text{test}}$. The testing accuracy rate $R$ is expressed as follows:

$$R = \frac{N_{\text{TtoT}} + N_{\text{FtoF}}}{N}. \tag{3}$$

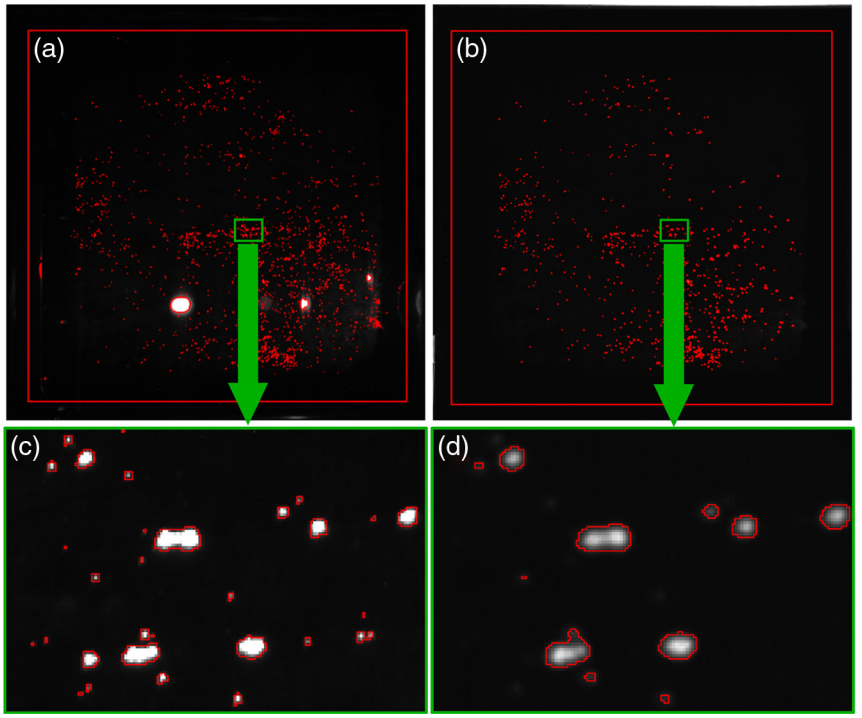


**Fig. 11** Online and offline FODI images. (a) Online sites, which include true and false sites. (b) Offline sites, which include only true sites in the FODI offline image. (c) Enlarged view of the green frame in Fig. 11(a). (d) Enlarged view of the green frame in Fig. 11(b).

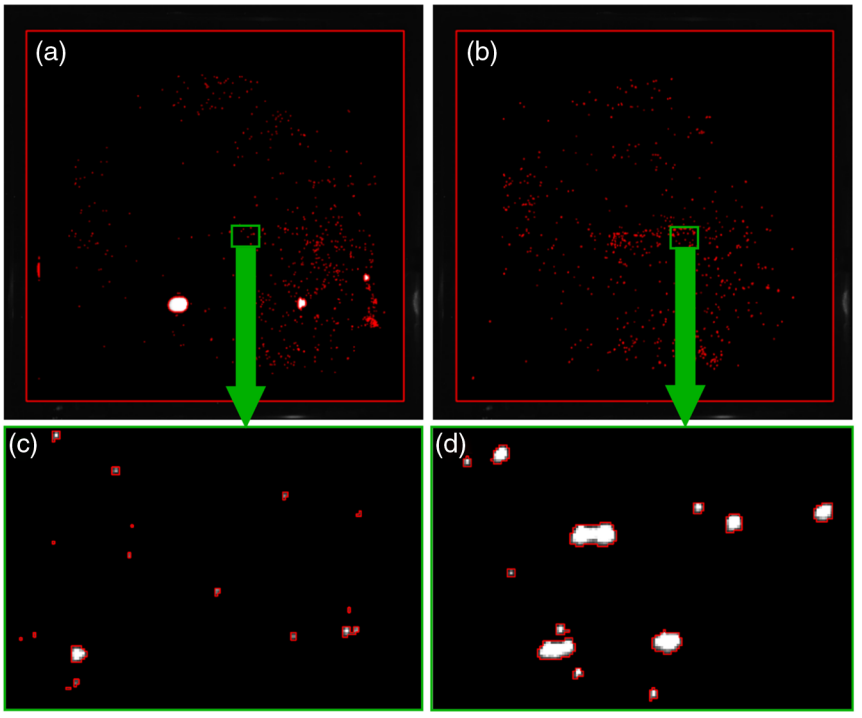


**Fig. 12** Sample sites in FODI online image. (a) Only false sample sites in the FODI online image. (b) Only true sample sites in the FODI online image. (c) Enlarged view of the green frame in Fig. 12(a). (d) Enlarged view of the green frame in Fig. 12(b).

Here, $N_{\mathrm{TtoT}}$ is the number of true sites accurately classified, $N_{\mathrm{FtoF}}$ is the number of false sites accurately classified, and $N$ is the number of testing data sets.

We wrote our codes using the Halcon software (MVTec Software GmbH, Munich, Germany) to perform the above steps. In our training and testing samples, which include true sites and all types of false sites, the damage size range is 50 to 1200 $\mu$m. As shown in Table 4, the testing accuracy rate of the K-ELM with 16 features and the optimized parameters $(C^*, \gamma^*)$ is verified on the testing data set.

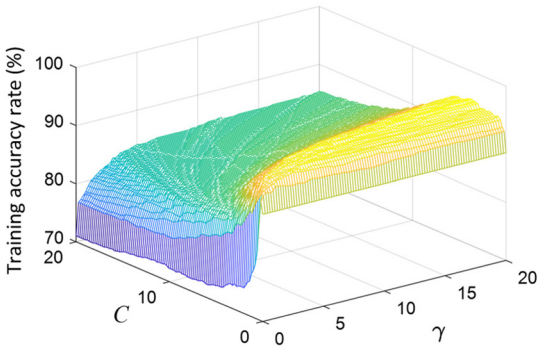


**Fig. 13** Training accuracy rate of the K-ELM for different parameters $(C, \gamma)$.

**Table 4** Testing results of different classifiers on the vacuum isolator.

| Training data | Testing data | Classifiers | | | | |
|---|---|---|---|---|---|---|
| 368(T) 335(F) | 368(T) 336(F) | EDT1 | EDT2 | BPNN | SVM | K-ELM |
| Testing accuracy rate | | 90.00% | 94.29% | 92.43% | 96.91% | 97.46% |
| Training time | | 1.17 s | 1.30 s | 727.61 ms | 72.35 ms | 24.40 ms |
| Testing time | | 0.23 s | 0.24 s | 566.20 ms | 14.59 ms | 16.38 ms |

For comparison, we test the accuracy of the ensemble of decision trees with 12 features (denoted as EDT1) proposed in Ref. 15 and the ensemble of decision trees with 16 features (denoted as EDT2) proposed in this paper. Lastly, we also provide the classification results obtained using the BPNN and SVM methods in Table 4 (T: true sites, F: false sites).

## 4 Discussion

Overall, the results in Table 4 show that the testing accuracy rate of the K-ELM is the highest among these classifiers. From the perspective of training speed, the speed of the K-ELM is the fastest, which is due to the structure and characteristics of the algorithm, regarding which this paper offers no further discussion. The rapid training speed helps to reduce the time required to obtain the optimal classifiers. From the perspective of testing speed, the speed of the K-ELM is only slightly lower than that of the SVM and higher than that of all other classifiers. The rapid testing speed has important practical significance in terms of practical application.

Further analysis shows that because the testing accuracy rate of EDT2 is higher than that of EDT1, the 16 features presented in this paper are more effective in characterizing the difference between true and false damage. Thus, it is meaningful to analyze the optical principle of true and false damage. In addition, choosing the appropriate classifier can further improve the classification accuracy, as well as help to reduce the training time and testing time.

## 5 Conclusions

This paper presents an automatic classification method for the identification of true and false damage sites in an FODI online image, and it solves the problem of false damage interference, especially from Att-type false damage, which cannot be identified by the human eye and regarding which the previous literature in the field of damage online inspection makes little reference. This method accurately aligns the FODI system inspection results with the FOA damage condition, thereby improving authenticity and credibility. First, stray light caused by edge illumination is an important factor of the generation of false damage sites, as determined by the Monte Carlo ray-tracing method. Second, the FDTD and Fourier optic AST for Maxwell's equations are used to analyze the far-field light intensity characteristics of the pit and attachments, and the multiparameter-characterized differences in light intensity distributions on CCD surfaces are analyzed theoretically. The multiparameter-characterized differences provide a key theoretical basis for selecting features in machine learning. Finally, the K-ELM model is used to realize intelligent classification of true and false damage sites based on feature vectors consisting of multiple parameters. The experimental results show that the 16 features proposed in this paper can improve the classification accuracy of true and false damage sites, including false damage site types such as HR, DC, RD, and Att. In the field of damage online inspection, the K-ELM model is also more suitable for the classification of true and false sites than the existing methods. The accuracy rate of the K-ELM classifier is 97.46% for the testing data set, for which the damage size range is 50 to 1200 $\mu$m, and its calculation speed is relatively good, thus meeting the technical requirements for the FODI online system.

### Acknowledgments

This work was supported by the National Natural Science Foundation of China (Nos. 51275120 and 61275096) and the Fundamental Research Funds for the Central Universities (No. HIT.NSRIF.2013012).

### References

1. Z. M. Liao et al., "Optics damage modeling and analysis at the National Ignition Facility," *Proc. SPIE* **9237**, 92370Y (2014).
2. B. Bussière et al., "Importance of surface topography on pulsed laser-induced damage threshold of sapphire crystals," *Sci. Rep.* **7**(1), 1249 (2017).
3. P. Wang et al., "Luminescence in the fluoride-containing phosphate-based glasses: a possible origin of their high resistance to nanosecond pulse laser-induced damage," *Sci. Rep.* **5**, 8593 (2015).
4. L. Gallais et al., "Wavelength dependence of femtosecond laser-induced damage threshold of optical materials," *J. Appl. Phys.* **117**(22), 223103 (2015).
5. E. Feigenbaum, N. Nielsen, and M. J. Matthews, "Measurement of optical scattered power from laser-induced shallow pits on silica," *Appl. Opt.* **54**(28), 8554–8560 (2015).
6. E. Feigenbaum, S. Elhadj, and M. J. Matthews, "Light scattering from laser induced pit ensembles on high power laser optics," *Opt. Express* **23**(8), 10589–10597 (2015).
7. Y. Li et al., "Generation of scratches and their effects on laser damage performance of silica glass," *Sci. Rep.* **6**, 34818 (2016).
8. L. M. Kegelmeyer et al., "Automated optics inspection analysis for NIF," *Fusion Eng. Des.* **87**(12), 2120–2124 (2012).
9. A. Conder et al., "Final optics damage inspection (FODI) for the National Ignition Facility," *Proc. SPIE* **7797**, 77970P (2010).
10. F. Bo et al., "Segmentation of small defects in final optics damage online inspection images," in *Int. Conf. on Image Analysis and Signal Processing*, pp. 1–4 (2012).
11. L. M. Kegelmeyer et al., "Local area signal-to-noise ratio (LASNR) algorithm for image segmentation," *Proc. SPIE* **6696**, 66962H (2007).
12. D. A. Alessi et al., "Picosecond laser damage performance assessment of multilayer dielectric gratings in vacuum," *Opt. Express* **23**(12), 15532–15544 (2015).

13. R. A. Negres et al., "Growth model for laser-induced damage on the exit surface of fused silica under UV, ns laser irradiation," *Opt. Express* **22**(4), 3824–3844 (2014).
14. M. L. Spaeth et al., "Optics recycle loop strategy for NIF operations above UV laser-induced damage threshold," *Fusion Sci. Technol.* **69**(1), 265–294 (2016).
15. G. M. Abdulla et al., "Effective and efficient optics inspection approach using machine learning algorithms," *Proc. SPIE* **7842**, 78421D (2010).
16. P. A. Baisden et al., "Large optics for the National Ignition Facility," *Fusion Sci. Technol.* **69**(1), 295–351 (2016).
17. J. D. Lindl et al., "Overview: development of the National Ignition Facility and the transition to a user facility for the ignition campaign and high energy density scientific research," *Fusion Sci. Technol.* **69**(1), 1–24 (2015).
18. M. Sozet et al., "Laser damage density measurement of optical components in the sub-picosecond regime," *Opt. Lett.* **40**(9), 2091–2094 (2015).
19. R. N. Raman et al., "Damage on fused silica optics caused by laser ablation of surface-bound microparticles," *Opt. Express* **24**(3), 2634–2647 (2016).
20. L. Li et al., "Automated discrimination between digs and dust particles on optical surfaces with dark-field scattering microscopy," *Appl. Opt.* **53**(23), 5131–5140 (2014).
21. E. Feigenbaum et al., "Laser-induced hertzian fractures in silica initiated by metal micro-particles on the exit surface," *Opt. Express* **24**(10), 10527–10536 (2016).
22. S. G. Demos et al., "Mechanisms governing the interaction of metallic particles with nanosecond laser pulses," *Opt. Express* **24**(7), 7792–7815 (2016).
23. E. Cambria et al., "Extreme learning machines [trends & controversies]," *IEEE Intell. Syst.* **28**(6), 30–59 (2013).
24. F. Benot et al., "Feature selection for nonlinear models with extreme learning machines," *Neurocomputing* **102**, 111–124 (2013).
25. G. B. Huang et al., "Extreme learning machine for regression and multiclass classification," *IEEE Trans. Syst. Man Cybern. Part B* **42**(2), 513–529 (2012).
26. G. B. Huang, "What are extreme learning machines? Filling the gap between frank Rosenblatt's dream and John von Neumann's puzzle," *Cognit. Comput.* **7**(3), 263–278 (2015).
27. G. B. Huang, "An insight into extreme learning machines: random neurons, random features and kernels," *Cognit. Comput.* **6**(3), 376–390 (2014).

**Fupeng Wei** is a PhD student at Harbin Institute of Technology, China. He received his BS degree from Henan University of Science and Technology, China, in 2011. He received his MS degree from Zhengzhou University, China, in 2013. His research interests include tiny defect detection on large aperture optics, image processing, and machine learning.

**Fengdong Chen** is an associate professor at Harbin Institute of Technology, China. He received his BS degree from China University of Petroleum, China, in 2000. He received a PhD from Harbin Institute of Technology, China, in 2009. His research interests include precision instruments and testing technology and visual detection and measurement.

**Bingguo Liu** is an associate professor at Harbin Institute of Technology, China. He received his BS, MS, and PhD degrees from Harbin Institute of Technology, China, in 1998, 2004, and 2009, respectively. His research interests include precision instruments and testing technology, laser measurement technology, and visual detection technology.

**Zhitao Peng** is a professor and the director of the Department of Laser Technology and Engineering, China Academy of Engineering Physics, China. He received his PhD from China Academy of Engineering Physics, China, in 2011. His research interests include optical engineering, laser measurement technology, and visual detection technology.

**Jun Tang** is an associate professor and the group leader at the Department of Laser Technology and General Research, China Academy of Engineering Physics, China. He received his MS degree from Harbin Institute of Technology, China. His research interests include optical engineering, laser measurement technology, and visual detection technology.

**Qihua Zhu** is a professor and the director of the Science and Technology Commission, China Academy of Engineering Physics, China. He received his PhD from China Academy of Engineering Physics, China. His research interests include optical engineering, nuclear physics, and visual detection technology. He is responsible for the SG-III laser facility.

**Dongxia Hu** is a professor and the director of the Department of Laser Technology and General Research, China Academy of Engineering Physics, China. He received his PhD from China Academy of Engineering Physics, China. His research interests include optical engineering and nuclear energy science and engineering. He is the winner of the China Youth Five Four Medal in 2017. He is responsible for the overall integration of SG-III laser facility.

**Yong Xiang** is an associate professor and the group leader at the Department of Laser Technology and Engineering, China Academy of Engineering Physics, China. He received his MS degree from Harbin Institute of Technology, China, in 2011. His research interests include precision instruments, testing technology, and optical engineering.

**Nan Liu** is an associate professor and the project administrator of the SG-III laser facility, China Academy of Engineering Physics, China. He received his MS degrees from Harbin Institute of Technology, China, in 2013. He is mainly engaged in the research of high-power solid laser amplifier technology.

**Zhihong Sun** is a professor at the Department of Laser Technology and Engineering, China Academy of Engineering Physics, China. She is mainly engaged in optical detection and photonic crystal research.

**Guodong Liu** is a professor in Harbin Institute of Technology, China. He received his BS, MS, and PhD degrees from Harbin Institute of Technology, China, in 1996, 1998, and 2005, respectively. His research interests include precision instruments and testing technology, laser measurement technology, and visual detection technology.